The Astronomical Journal, 137:4091–4099, 2009 May doi:10.1088/0004-6256/137/5/4091

DESIGN AND TEST OF AN INSTRUMENT FOR MEASURING MICROTHERMAL SEEING ON THE MAGDALENA RIDGE

A. M. Jorgensen[1], D. A. Klinglesmith III[2], J. Speights[3], A. Clements[3], and J. Patel[3]
[1] Electrical Engineering Department, New Mexico Institute of Mining and Technology, 801 Leroy Place, Socorro, NM 87801, USA
[2] Magdalena Ridge Observatory, New Mexico Institute of Mining and Technology, 801 Leroy Place, Socorro, NM 87801, USA
[3] Physics Department, New Mexico Institute of Mining and Technology, 801 Leroy Place, Socorro, NM 87801, USA
Received 2008 June 3; accepted 2008 December 18; published 2009 March 26

ABSTRACT

We have constructed and operated an automated instrument for measuring ground-level microthermal seeing at the Magdalena Ridge Observatory (MRO). The MRO is located at an altitude of 10500′ in the Cibola National Forest in New Mexico, USA. It is the planned site for the MRO Optical Interferometer (MROI) planned for up to 10 collecting elements, each with a diameter of 1.4 m, and baselines eventually up to approximately 400 m. As part of the preparation for construction we deployed a system to characterize the ground-level seeing across the observatory site. The instrument is built largely of off-the-shelf components, with only the sensor head and power supply requiring electronic board assembly. Even in those cases the board architecture is very simple. The first proof-of-concept system was deployed for several weeks in the autumn of 2004, and has since undergone several iterations. The latest configuration operates entirely off batteries, incorporates wireless data acquisition, and is thus able to operate in an area with no shelter, power, or communications. In this paper we present the design of the instrument, and show initial data. The microthermal tower has four sensor pairs at heights from 0.8 to 4.41 m, significantly lower than other microthermal experiments, because of the need to characterize the seeing near the ground. We find significant variation in the contribution of this range of heights to the seeing, contributing up to 0.″3 of the seeing at some times and only 0.″02 at other times. The individual sensor power spectra have a slope in the range of 1.4–1.5, which is lower than the 1.67 slope predicted by Kolmogorov turbulence theory. We measure the well known effect of improved seeing immediately around sunset. While we find significant variation in the microthermal seeing, we did not find a pattern of corresponding variations in weather conditions, suggesting that a complicated set of factors control microthermal turbulence.

Key words: atmospheric effects – instrumentation: miscellaneous – site testing

1. INTRODUCTION

Microthermal measurements are used to determine the contribution of ground-level turbulence to astronomical seeing. In the case of the Magdalena Ridge Observatory Interferometer (MROI) the results were used in the analysis of the cost-benefit trade-off of placing the telescopes above ground level. Placing a telescope higher above the ground will involve additional cost, but may also result in improved seeing. The question that we were seeking to answer was how great the improvement would be at a greater height, which could be used to assess whether the additional expense of raising the telescopes could be justified.

Because of turbulence air temperatures vary on the timescale of tenths or hundredths of seconds. The temperature variations on these timescales is on the order of a degree or less. Thus a sensor is needed which can measure the air temperature sufficiently rapidly and with sufficient sensitivity. It must have low thermal mass, and it must be possible to read it out a hundred times per second.

Microthermal seeing is often used in site characterization, and numerous results have been published using different instrument configurations. Marks et al. (1996) used microthermal measuring equipment similar to that of Vernin and Munoz-Tunon (1992) to measure the vertical seeing profile at the South Pole up to an altitude of 27 m. Marks et al. (1996) used sensors whose resistance varied with temperature. They found a large contribution from the ground level seeing. They found an average total seeing at the ground level of 0.″64, whereas it was 0.″46 measured in the 17–27 m section of the tower. Marks et al. (1996) also noted that sensors can tend to ice over in certain weather conditions, and that this will destroy the measurement because it increases the time constant to the point where relevant temperature fluctuations are no longer captured. They do remark, however, that these conditions were generally easy to identify in the data. Marks et al. (1999) expanded on this earlier work by including measurements from microthermal sensors flown on balloons.

Pant and Sagar (1998) presented a design for a microthermal measurement instrument based on a coil of nickel wire, and later presented the results of measurements with this instrument (Pant et al. 1999). They had pairs of sensors 1 m apart located at heights of 6, 12, and 18 m above the ground. Similarly to Marks et al. (1996), they found a large decrease in turbulence with altitude, and a significant decrease in seeing for heights of 6 m and higher above ground.

Our microthermal measurement instruments have evolved over several generations. However, common to them all is that they use very fast response thermocouples (TCs) as the sensing element. In Section 2, we present a brief overview of the theory describing microthermal turbulence and its relationship to astronomical seeing. In Section 3, we describe the instrument. In Section 4, we present some initial data and interpretations. While the ground-layer microthermal turbulence varied significantly over the time period we present in this paper, we did not find any obvious meteorological measurements that could explain this variation.

1.1. Relationship to the MROI

The purpose of this project was to provide information about the seeing very close to the ground, up to an altitude of

approximately 4 m. This would help in deciding whether the additional expense and complication of raising the telescopes above ground level could be justified. The system consisted of four towers each with four sensor pairs between 0.8 m and 4.41 m altitude. One tower was located at the nominal center of the planned array, and one at the end of each arm of the array. The two sensors at each height could then be used to measure C_T^2 and (using data from a nearby weather station) thus C_n^2 at that height, and then to estimate the contribution to the total seeing at that height. The towers were built to operate autonomously for long periods of time, weeks to months. An existing nearby weather station (800 m away) provided some weather data with which to correlate the measurements.

2. THEORY

Atmospheric seeing is caused by variations of the refractive index of the atmosphere. These refractive index changes are characterized by temperature fluctuations in the air. By measuring the temperature fluctuations it is possible to derive the fluctuations in the refractive index, and thus the contribution to atmospheric seeing of the air at the point of measurement.

Assuming a Kolmogorov spectrum for the atmospheric turbulence, the full width at half-maximum (FWHM) atmospheric seeing, in arcseconds, as a function of the path length of the light can be determined as

$$\epsilon_{\mathrm{FWHM}}(L) = 5.25\lambda^{-\frac{1}{5}} \left(\int_0^L C_n^2(l)dl \right)^{\frac{3}{5}}. \quad (1)$$

In this expression, C_n^2 is the refractive index structure constant, λ, is the wavelength of the light, in m, and l is the path of the light, also measured in m. For additional information about the derivation of this expression, see Marks et al. (1996), Dierickx (1992), and Roddier (1981). Seeing is cumulative, which means that the further the light travels through the atmosphere, the worse the seeing. L is zero at the top of the atmosphere, and has its maximum at the surface of the Earth. As an alternative to determining C_n^2 to the top of the atmosphere, we can assume (or measure) a value for the seeing at some altitude, compute the corresponding value of the integral at that altitude, and continue the integral with measured values for C_n^2. The refractive index structure constant is in turn related to the temperature structure constant, C_T^2, via

$$C_n^2 = \left(80 \times 10^{-6} \frac{P}{T^2} \right)^2 C_T^2, \quad (2)$$

where P and T are the atmospheric pressure and temperature, measured in mBar and K, respectively. The temperature structure constant is, for a Kolmogorov-type spectrum, related to the temperature structure function, $D_T(\vec{r})$, as

$$D_T(\vec{r}) = C_T^2 |\vec{r}|^{\frac{2}{3}}. \quad (3)$$

The temperature structure function is in turn computed as

$$D_T(\vec{r}) = \langle |T(\vec{r_0}) - T(\vec{r_0} + \vec{r})|^2 \rangle, \quad (4)$$

where $\langle\ \rangle$ indicates an average over time. The temperature structure function is the mean-squared variation of the difference between the temperature at two points separated by the horizontal vector $\vec{r}$. For a Kolmogorov spectrum, the magnitude of the variation is dependent only on the separation of the sensors, as long as this separation distance is between the inner scale and the outer scale, and characterized by a single value, C_T^2. We can thus infer the power in the Kolmogorov spectrum by measuring the mean-squared variation at only one separation between two sensors.

3. DESCRIPTION OF THE INSTRUMENT

In describing the instrument we will consider the sensors in Section 3.1, the data collection subsystem in Section 3.2, the communications subsystem in Section 3.3, the power subsystem for delivering clean power to the sensors and powering the other components in Section 3.4, calibration issues in Section 3.5, and instrument sensitivity in Section 3.6

3.1. Sensors

We use fast response TCs manufactured by Omega Engineering, Inc. (www.omega.com), the CO-2K. The TC leads are taped over for electrical isolation (Figure 1(b)), and to make the TC more resistant to damage by accidentally pulling the leads. A notch is cut in a rubber stopper, and the TC is glued inside it with rubber glue. The stopper is then glued inside an inverted plastic funnel, such that the TC junction extends a few millimeters above the funnel (Figure 1(d)). Inside the funnel is also mounted the amplifier board and a set of terminal blocks for connecting the analog data lines to the ADC (see Figure 1(c)). Figure 1(e) shows an assembled tower with four sensor pairs at different heights above the ground. The entire tower is 4.6 m tall, and the sensor pairs are separated horizontally by approximately 1.2 m from 0.8 m to 4.41 m height. Figure 2 shows the wiring diagram for the amplifier board. We used the low-noise OP-27 amplifier, and the resistors $R1 = 220\,\mathrm{K}\Omega$ and $R2 = 22\,\Omega$ were sized in order to obtain an amplification factor of 10^4. Finally, a capacitor ($C1 = 0.047\ \mu\mathrm{F}$) is added in order to limit the signal bandpass to the sample frequency. The inverted funnels are mounted on top of a base, and a cage of 1/2″ mesh is attached, then a top plate. These serve to protect the sensor head from weather and animals.

3.2. Data Collection

The signal from the sensor is transported to the data collection unit via a cable containing two individually shielded twisted pairs. One pair carries DC voltage power (−6V and +6V) for the amplifiers. The other pair carries ground and the return amplified signal from the sensor. These signals are sampled at 300 Hz using a Labjack UE9 analog-to-digital converter and controller (www.labjack.com). The Labjack unit has an Ethernet interface, and a custom program running on a remote Linux computer connects to the UE9 unit via TCP to retrieve the data stream. The custom program is available from the authors to any user wishing to duplicate the experiment. For eight sensors (four heights) the unit produces 46 bytes of data 300 times per second, for a total data rate of 14 kB s^{-1}. Only 16 bytes of data are collected from each packet and, together with time-tagging information, produce approximately 420 MB of data per day.

3.3. Communications

We decided to use a wireless data collection network for two reasons. First, we had the need to place towers several hundred meters from the nearest suitable location for a data collection computer. Ethernet cables are limited to 100 m in length,

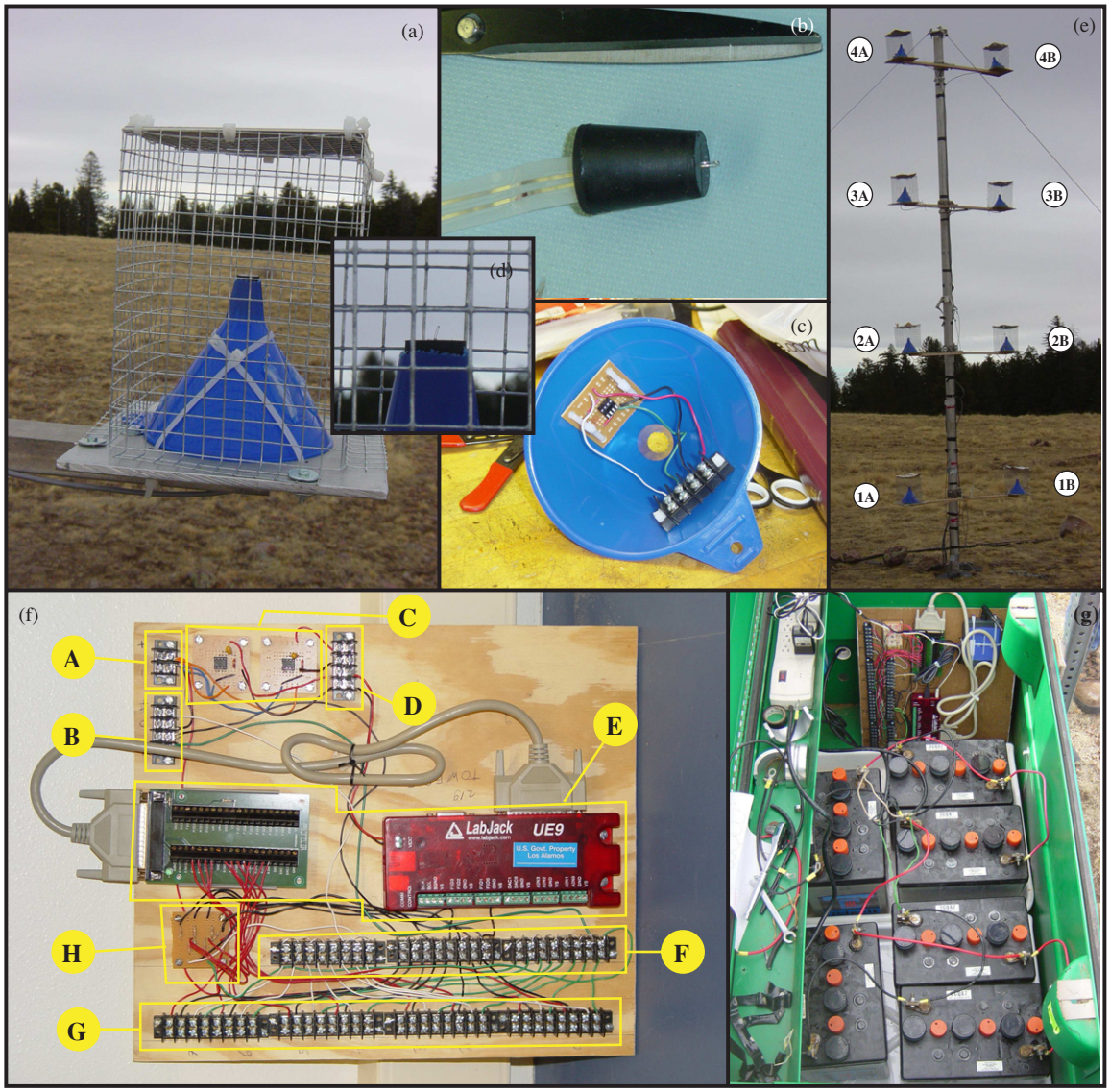

Figure 1. Photos of the hardware: (*a*) an assembled sensor in the field, (*b*) an insulated TC mounted in plug, (*c*) the inside of a sensor housing with amplifier board and external connector, (*d*) a close-up of the TC mounted at the top of the sensor assembly, (*e*) an entire tower, 15′ tall, (*f*) a data acquisition board [(A) 0–6 V input power for UE9 and radio, (B) −6to + 6 V input for sensor amplifiers, (C) 5 V voltage regulators for UE9 and radio, (D) a 5 V regulated outlet, (E) a UE9 data acquisition unit and auxiliary input board, (F) sensor power distribution points, (G) sensor connections (there are four screws for each sensor, providing ground, positive and negative voltage for the amplifier, and return voltage measurement), (H) a voltage monitoring board], (*g*) a battery power system.

and using them would require inserting repeaters in locations where there is no electrical power to supply them. Second, because the MRO site experiences frequent lightning storms, particularly during the summer monsoon season, wires which connect the outside and inside of buildings, or which extend over significant outdoor distances pose serious hazards to personnel and equipment. For this reason we chose to connect the data collection units and the data collection computer via an ad hoc 802.11b network. The 802.11b has a theoretical throughput of 1.3 MB s^{-1} compared to our requirement of 14 kB s^{-1} per tower. We used Linksys WET-11 wireless bridges, which we weatherproofed by placing them inside a sealed plastic paint bucket. Unobstructed, we have tested these radios to a range of 0.5 miles.

3.4. Power

There are two power systems. One power system supplies the sensors with −6V and +6V. The other power system supplies the Labjack UE9 data acquisition unit and the WET-11 wireless radio. For the sensor power system, we connected batteries in series, while for the data acquisition unit and the radio we connected batteries in parallel. A low-dropout voltage regulator produces a +5V output from the 6V car batteries to power the data acquisition unit and the radio, whereas the sensors were supplied directly from the batteries. In order to allow long-term unattended operation, the towers could be equipped with solar panels for charging of the batteries. We have not installed solar panel chargers, but they would clearly reduce the maintenance burden significantly. Without solar panels each tower requires attention approximately every three weeks. We took care in connecting all systems to a single ground point in order to minimize noise and interference. The UE9 also monitors the battery voltages. A photo of the battery system is shown in Figure 1(g), and a schematic diagram is shown in Figure 3.

3.5. Calibration Issues

There are few calibration issues related to this system. In the narrow range of temperatures differences between junction and

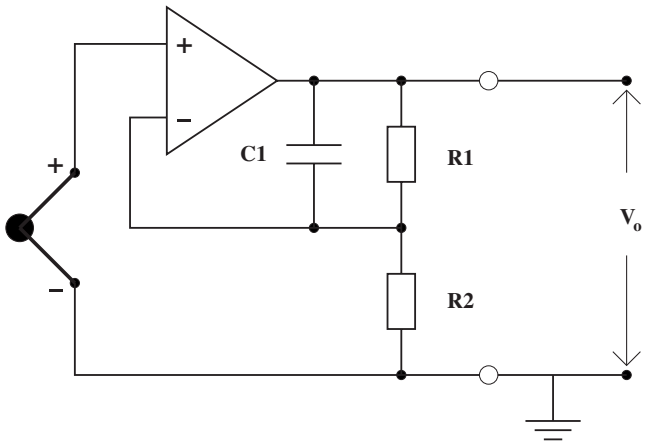

Figure 2. Schematic of the amplifier board. The TC is shown to the left.

reference (plus or minus 10 K), the TCs are highly linear to much better than 1% so that we can ignore the effects of nonlinearities. In that range they produce 39.5 μV K^{-1}. Their accuracy is also better than 1% according to the manufacturer. The second step is the amplification. We used 1% resistors which should result in an accuracy of better than a few percent. The last concern is the thermal time constant of the TCs. Variation in the thermal mass and proximity of objects with large thermal mass could affect the TC responses. The time constant can be measured from the power spectrum, and we did this routinely with the data. We also checked the calibration by placing sensors very close to each other and verifying that they recorded the same waveform. Figure 4 shows 20 s of data from a sensor pair. Panel (a) shows the time series, and panel (b) shows a scatter plot comparing the two. The sensors were placed very close together (within 2 cm of each other). From each trace we have subtracted an arbitrary offset. This offset exists because the reference junction temperature (where the TC is attached to the amplifier board) is not necessarily the same for the two sensors. This reference junction temperature only varies slowly however due to the much larger thermal mass of the junction. The offset is removed in the data analysis since we are only interested in the short-term variations. The correlation coefficient for a 1 hr interval of these data is $R = 0.93$.

Figure 5 shows histograms of the data after subtracting the 1 minute average, using the same data set as is plotted in Figure 4. In each panel the solid curve is the histogram of data from one data set whereas the dotted curve is the histogram of the measurements from the other sensor. Panel (a) shows 2 minutes of data, panel (b) shows 10 minutes of data, panel (c) shows 1 hr of data, and panel (d) shows 6 hr of data. The solid curve shows the histogram for one sensor and the dotted curve shows the histogram for the other sensor. Computing the histograms after subtracting longer-term averages is less interesting because on a longer timescale the reference level (which is set by the temperature of the junction) will vary in a manner which is dependent on sun angle, shadowing, placement of the amplifier chip inside the housing. Histograms can be used to verify the calibration. If the histograms are not identical (due, for example, to different values for the gain resistors), this will be apparent, and the sensors can be cross-calibrated by linear regression.

3.6. Sensitivity Calculation

Referring to Figure 2, we can see that the output MS noise is given by

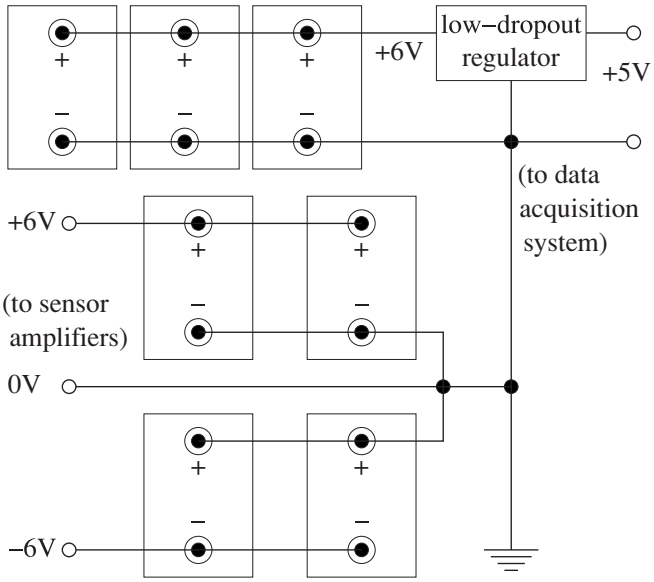

Figure 3. Schematic of the battery power system for the data acquisition and radio system and for the sensor amplifiers.

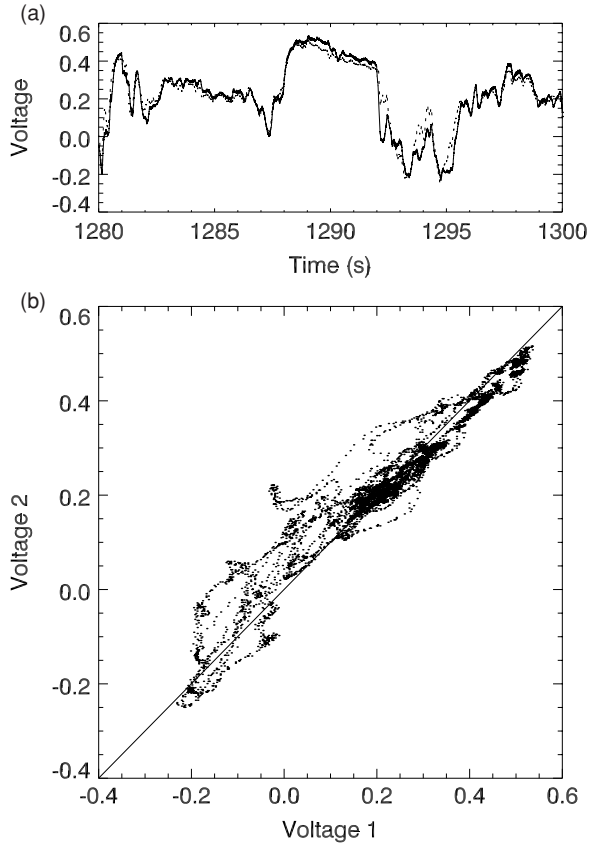

Figure 4. Verification of calibration by placing sensors very close together. Two sensor were placed facing each other such that the sensor heads were separated by less than 2 cm; (a) time series; (b) scatter plot.

$$\langle v_o^2 \rangle = [K^2 e_{\rm na}^2 + 4kT(R_1 + R_2)T]B \qquad (5)$$

where we assume that the thermal noise in the TC is negligible compared to the input noise of the amplifier. Here $K = 10^4$ is the amplifier gain, B is the bandwidth (150 Hz), $e_{\rm na} = 3$ nV/$\sqrt{\rm Hz}$ is the input noise of the amplifier, k is the Boltzmann constant, and $T \approx 273$ K is the ambient temperature. Inserting known

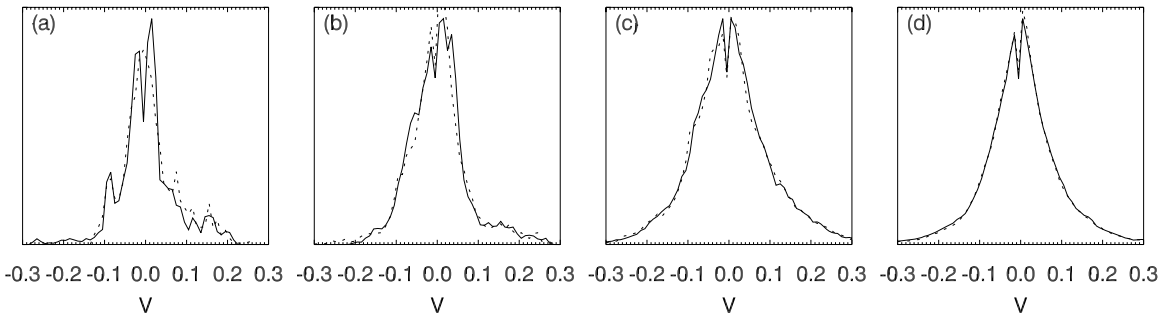

Figure 5. Histograms of the calibration data. The solid curve shows the histogram for one sensor, whereas the dotted curve shows the histogram for the other sensor. In each histogram the 1 minute average is subtracted from the data before binning. Deviations from long-term averages are less interesting. A different length of data is binned in each panel: (*a*) 2 minutes; (*b*) 10 minutes; (*c*) 1 hr; (*d*) 6 hr.

Table 1
Table of Sensor Parameters

Parameter	Value
Sensor Pair Separation	1.0 m
ADC Range	−5 V to +5 V
ADC Levels	4096
Temperature Range	−12.5 K to 12.5 K
RMS Electronic Noise	4.5 mV
Equiv. Temperature	11 mK
Digitization Interval	2.4 mV
RMS Digitization Noise	0.69 mV
Equiv. Temperature	1.7 mK
Sampling Frequency	300 Hz
Sensor Time Constant	∼0.05 s
Amplifier Bandwidth	150 Hz

values, we obtain

$$\sqrt{\langle v_o^2 \rangle} = 4.5\,\mathrm{mV}. \tag{6}$$

The ADC digitizes the −5 *V* to +5 *V* range at 12 bits, which is equivalent to a digitization interval of $\Delta = 2.4\,\mathrm{mV}$, and an rms digitization noise of

$$\sqrt{\langle v_d^2 \rangle} = \frac{\Delta}{\sqrt{12}} = 0.69\,\mathrm{mV}. \tag{7}$$

With a voltage to temperature conversion factor of 2.5 K V^{-1}, the thermal and digitization noise are 11.25 mK and 1.73 mK, respectively. The time constant for the sensor is approximately $\tau = 0.05$s, and this will be discussed in Section 4.4. Table 1 summarizes the sensor and measurement system performance parameters.

4. INITIAL RESULTS

4.1. Raw Data

The raw data output from the instrument are time series of voltages, recorded at 300 Hz. This corresponds to approximately 2.6×10^7 measurements per day. Figure 6 shows the raw data for a 2 hr nighttime interval. In each panel are plotted the voltages for the two sensors at the same level. The solid curves represent the median, and the dotted curves the quartiles for each 1 minute interval. The distance between the quartiles is typically larger at lower altitude than at higher altitude. This is because there is typically greater turbulence at lower altitude than at higher altitude.

In the plots we have added an offset to one or both of the sets of traces to separate them. The measured offsets depend on the temperature difference between the TC and the circuit boards. At night when the temperature varies slowly this offset should be almost zero, but can be different from zero when the ambient temperature is changing. Regardless, this offset is not used in the data analysis as the low-frequency component of the data is subtracted during the analysis step.

It is interesting to note that at greater heights the voltage median and quartiles are more similar for the two pairs than they are at lower heights. The likely reason for this is that very close to the ground the direct interaction of the turbulence eddies with the ground and anything on the ground tends to be greater than at greater altitude. In other words, the two sensors near the ground may be measuring airmasses with slightly different characteristics because of this local interaction. This suggests that in future experiments it may be worth considering placing at least the smaller altitude sensors closer together. This also makes the measurement that much more local and susceptible to local effects. However, this may be desirable under some circumstances, for instance the mapping of the turbulence properties of a telescope dome on a cubic meter scale or less. It would also be interesting to deploy sensors with multiple separations in order to understand how this affects the spatial turbulence power spectrum.

4.2. Temperature Structure Constant

Figure 7 shows a plot of the temperature structure constant for each height above the ground from approximately sunset to sunrise on two consecutive nights. The values are computed on a 1 minute basis. We chose the value of 1 minute after some experimentation. The interval must be long enough to capture the full range of temperature variations. It must be significantly longer than the typical timescale for temperature variation. We must also be able to properly subtract the voltage baseline over the interval. We found that values from less than 1 minute up to an hour fulfilled these criteria, but that values in the short end of that range allowed us to better study temporal variations, and are also more appropriate for studying the atmospheric temperature variations, as discussed in Section 3.5.

First, the measured voltages must be converted to temperature. The TCs produce a voltage of 39.5 μV K^{-1}, which is amplified by a factor of 10^4. Thus, we have approximately 2.5 K V^{-1}. Next, we take the difference between sensors at each height. Because the slowly varying baseline is arbitrary, we subtract it separately in each 1 minute sequence (approximately 18,000 values) to produce a zero-mean time series for each 1 minute interval. Remember that the source of this baseline is the temperature difference between the TC junction and the

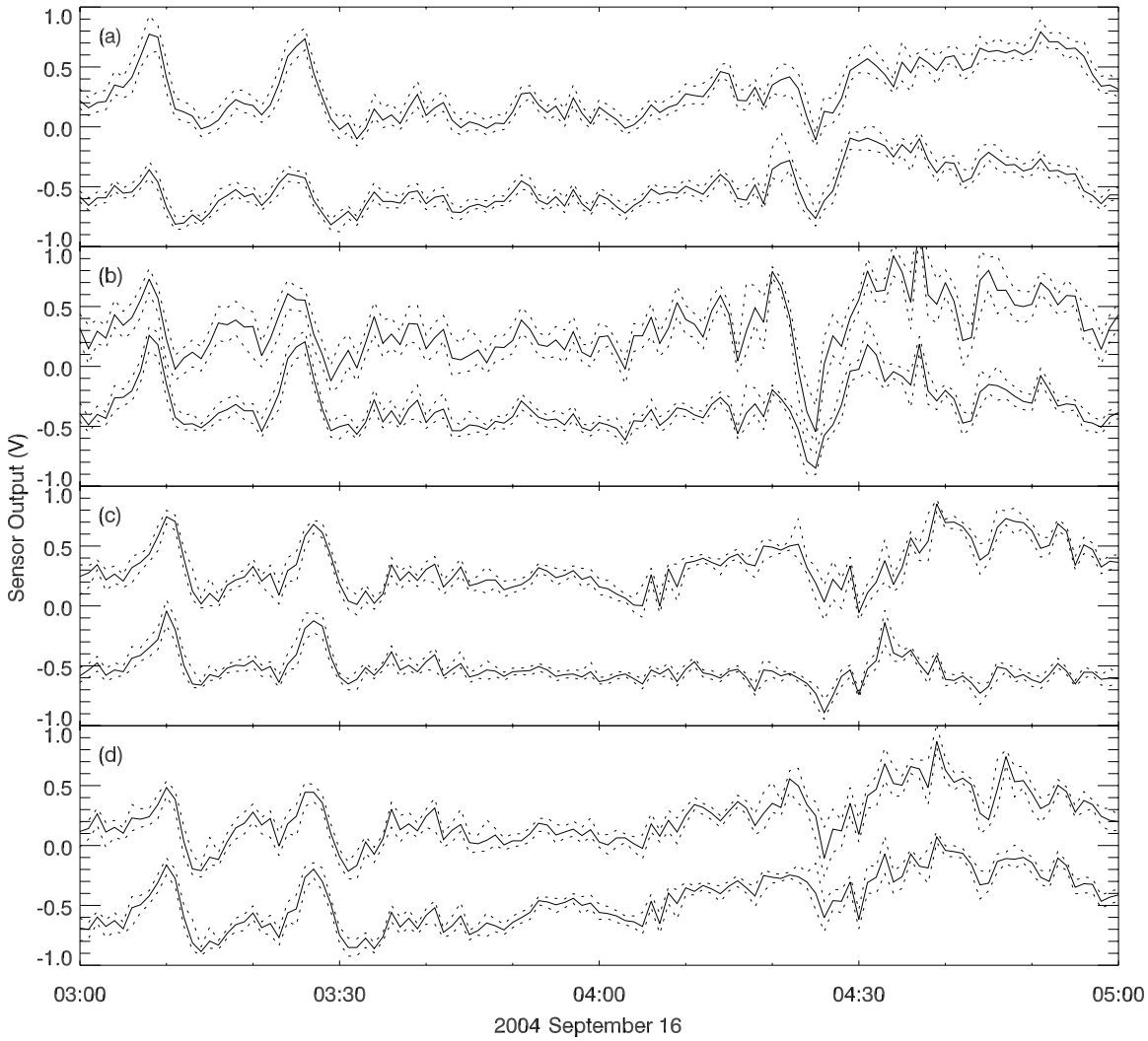

Figure 6. Raw voltages from a single tower. Panels (*a*)–(*d*) are data from the lowest to highest sensors, respectively. In each panel the two solid curves are the 1 minute median of voltages measured, and the dotted curves are the 50 and 75 percentiles. An arbitrary offset has been applied to plot the two sets of curves together and without overlap.

amplifier chip. Our instrument only measures the difference between the amplifier chip and the junction, not absolute temperature. We are assuming that the important temperature variations occur on a timescale short compared with the 1 minute averaging interval, and that the average temperature is the same at the two sensors. Thus, the temperature difference should have zero mean on a 1 minute timescale, and we subtract any nonzero mean to produce a zero-mean time series. The mean-squared of that zero-mean time series is what is plotted in Figure 7. The gap from approximately 21:30 to 22:30 in Figure 7(a) is an interval of bad data. (The earliest version of the instrument had occasional problems with bad connectors, a problem easily spotted in the data by the amplifier output being stuck at either high or low rail. This problem was corrected in later versions of the instrument by using screw terminals for connections, as shown in the photos in Figure 1.)

The propagated uncertainty in each 1 minute value of C_T^2 is

$$\frac{\sigma\left(C_T^2\right)}{C_T^2} = \sqrt{\frac{8q}{NC_T^2}} \tag{8}$$

where $q = 2.4$ mV is the digitization step size, and $N = 18 \times 10^3$ is the number of measurements combined. For $C_T^2 \in [0.01; 1.0]\, K^2$ it evaluates to a relative uncertainty of 0.013%–0.13%. Clearly, the uncertainty in the value of gain resistors, 1%, dominates the uncertainty of the C_T^2 values.

To help in seeing structure, we have smoothed the data in these plots with an 11 minute window. We notice a number of different patterns. For example, all traces drop sharply immediately around sunset (intervals A and E in Figure 7). Before midnight on the 15th the three lower sensor pairs track each other before the sensor pair at 3.23 m shifts (interval B) to track the top sensor pair (interval C). Then suddenly at 04:30 on the 16th there is a short period of high turbulence for approximately 15 minutes (interval D) before the turbulence pattern returns to its prior configuration. During the first half of the night after the 16th the turbulence pattern is stratified with much lower C_T^2 at greater heights than at lower heights (intervals F and G). Then after midnight (beginning at 00:45 on the 17th) the turbulence becomes more isotropic (interval H). We expect that the different turbulence patterns correspond to different weather patterns. However, examination of data from a weather station located approximately 800 m away shows no obvious relationship between weather conditions and turbulence conditions.

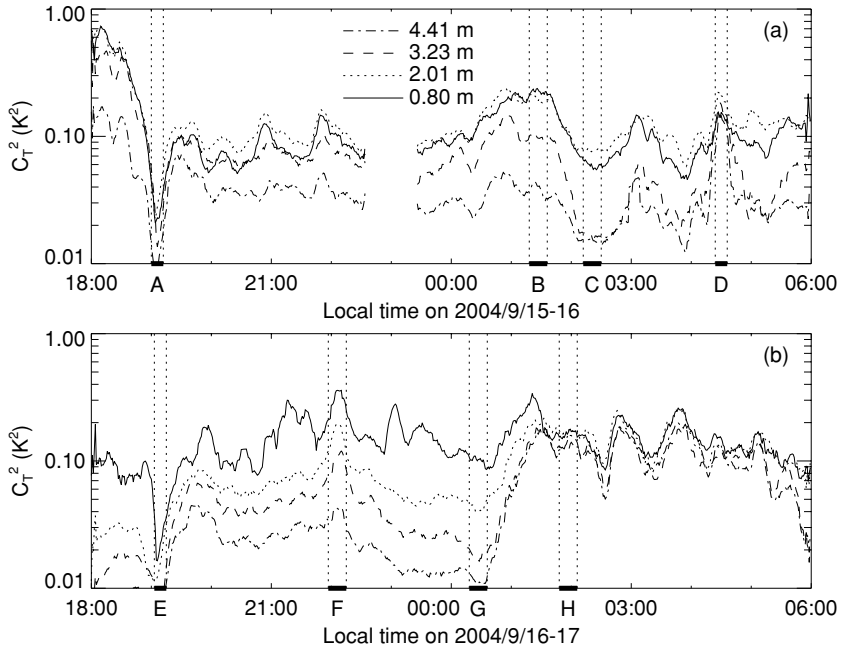

Figure 7. C_T^2 for the four different sensor pair heights on (*a*) the night between September 15 and 16, and (*b*) the night between September 16 and 17. C_T^2 values have been smoothed with an 11 minute window to allow longer-term time variations to stand out.

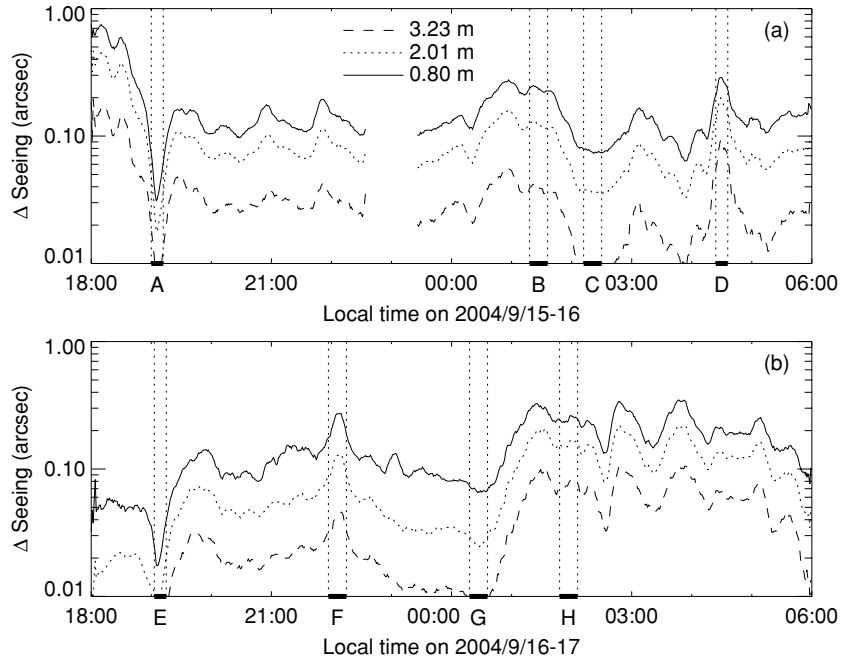

Figure 8. Seeing difference between top sensor pair and each of the three lower sensor pairs as a function of time for the C_T^2 data shown in Figure 7 for (*a*) the night between September 15 and 16, and (*b*) the night between September 16 and 17.

4.3. Seeing as a Function of Height

Figure 8 shows the seeing difference as a function of height in a format nearly identical to Figure 7. This plots shows the difference in seeing between the top sensor pair and each of the other sensor pairs. Figure 9 shows C_T^2 and the seeing difference as a function of height for the eight intervals marked in Figure 8. The seeing is computed using Equation (1). The 1% uncertainty from the C_T^2 measurements propagates, as well as uncertainty in the determination of atmospheric pressure and temperature (estimated at 1% also), so that C_n^2 has an estimated uncertainty of 2% on the measured baseline. It is important to realize that Equation (1) assumes a Kolmogorov spatial turbulence spectrum, consistent with assumptions in previous published work. It is not immediately possible to verify this assumption using these data. Measuring the shape of the spatial power spectrum requires the use of sensors at different separations. It is difficult to estimate what uncertainty might be associated with the assumption of a Kolmogorov spatial power spectrum. We believe that this uncertainty has both random and systematic components. It is also possible that non-Kolmogorov effects are more significant at the lower sensors pairs.

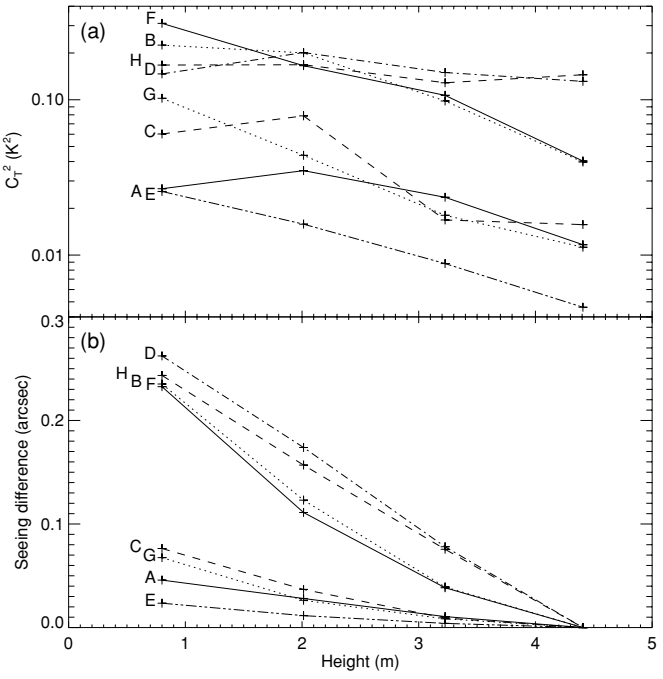

Figure 9. (*a*) C_T^2 as a function of altitude for the 8 intervals A through H labeled in Figure 7. (*b*) Computed seeing difference as a function of altitude, assuming a 1″ seeing at the top sensor.

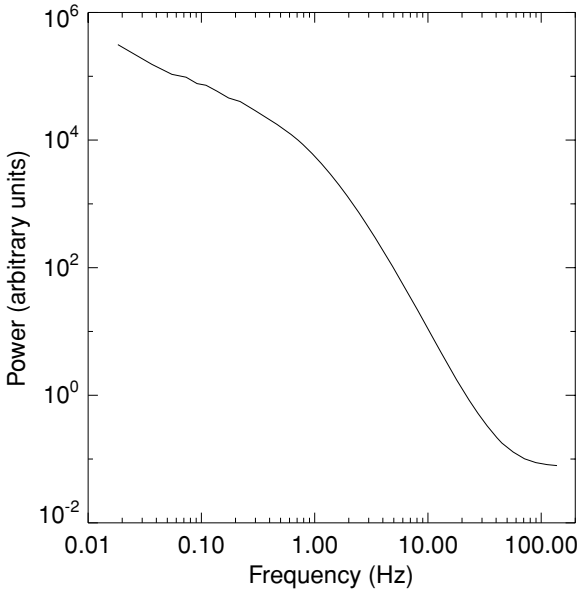

Figure 10. Power spectrum of the signal measured by a single sensor. Note the break in the spectrum around 1 Hz, as well as the noise floor apparent above 30 Hz.

In order to compute the seeing (and even just the change in seeing) we need to assume a value for the integral of C_n^2 from the top of the atmosphere to the top sensor pair. Based on previous optical seeing measurements at the site, we choose a value of the integral corresponding to a value of the seeing of one arc second at the top sensor pair. The choice for the seeing at the top sensor makes only little difference in determining the difference in seeing values between the top and the bottom sensor. Note that around sunset, which corresponds to regions A and E in Figures 7 and 8, the turbulence is very small, and the change in seeing from the top to the bottom sensor is also very small. This is a well-known phenomenon effect of good seeing immediately around sunset when up- and down-flowing energy balance each other.

Around sunset the measured seeing difference is very small, only a few hundredths of an arcsecond. Generally during the two nights we measured a seeing difference of approximately 0.″1–0.″2, except for the second half of the night after the 16th where we measured seeing difference values in the range 0.″2–0.″3. Since we only measured the turbulence amplitude up to a height of 4.41 m, we do not know what the total seeing is and thus not what fraction of the seeing is created below the top sensor. However, if we assume a median seeing at the site of 1″, it is not unreasonable to estimate very approximately that the seeing difference between the top and bottom sensors does not normally contribute more than about 20%. However, this number will need to be confirmed by subsequent work.

4.4. Sensor Time Constant

We can use the power spectrum of the individual sensors to determine the sensor time constants via the procedure outlined by Short et al. (2003). The spectrum in Figure 10 can be represented by the expression

$$P = a + b\frac{\nu^{-\beta}}{1 + (2\pi\nu\tau)^2} \quad (9)$$

Table 2
Average Power Spectrum Slopes and Sensor Time Constants, for Each Sensor

Sensor	β			τ (s)		
	Median	Average	σ	Median	Average	σ
1A	1.40	1.37	0.46	0.048	0.077	0.14
1B	1.36	1.35	0.43	0.048	0.077	0.14
2A	1.45	1.36	0.47	0.045	0.078	0.12
2B	1.46	1.39	0.47	0.045	0.074	0.14
3A	1.49	1.38	0.52	0.043	0.059	0.14
3B	1.47	1.40	0.43	0.045	0.066	0.10
4A	1.50	1.41	0.43	0.045	0.061	0.09
4B	1.47	1.39	0.43	0.046	0.070	0.10
Avg	1.45	1.38		0.047	0.070	

where a is the white noise floor in the measurement (digitization or electronic noise in the measurement process), b is a scaling factor, β is the spectrum slope, and τ is the sensor time constant. For a Kolmogorov spectrum the value of β is $\frac{5}{3}$. Fitting this spectrum model to data with a, b, β, and τ as free parameters we obtain the values in Table 2.

We can compare the values for β in Table 2 with the values obtained by Short et al. (2003). They had measurements over a wider range of heights (9–70 feet) than our 0.8 m to 4.41 m. At the lowest heights, which correspond to our higher sensors, they observe values generally in the range 1.65–1.75, compared to our values of 1.45. At low altitude they observed little variation with wind speed. At the highest altitude they measured values from 1.28 at zero wind speed up to values of 1.64 at 8 m s^{-1}. We do not have measurements under comparable conditions. In general, we did not see any variation with wind speed of the mean of either β or τ. Short et al. (2003) measured a variation of the sensor response time constant, τ, with a time constant of 0.15 s at zero wind speed, decreasing to 0.05 s at a wind speed of 10 m s^{-1}.

5. CONCLUSION

We have designed and constructed a simple inexpensive microthermal turbulence monitor with wireless data acquisition

and battery operation suitable for operating in a remote environment. The system is built using off-the-shelf components, and makes measurements at four levels from 0.8 m to 4.41 m above the ground. The individual sensors have a response time constant of approximately 0.05 s. We have operated the system at the Magdalena Ridge Observatory in New Mexico, USA, and shown the initial results. On the first two nights of observation we found a wide variation in turbulence conditions, with sometimes very steep gradients, and sometimes uniform turbulence across the height range. The measured turbulence contributed only a few hundredths of an arcsecond immediately around sunset, while during the night the contribution more typically ranged between 0.″1 and 0.″3.

The Magdalena Ridge Observatory (MRO) is funded by Agreement No. N00173-01-2-C902 with the Naval Research Laboratory (NRL). The MROI is hosted by the New Mexico Tech Institute of Mining and Technology (NMT) at Socorro, NM, USA. This work was also supported by the U.S. Department of Energy. The authors thank E. C. Downey for useful discussions, and Craig Wallace-Keck for invaluable assistance in installing and maintaining the equipment. The authors also thank the referee for very helpful suggestions.

REFERENCES

Dierickx, P. 1992, J. Mod. Opt., 39, 569
Marks, R. D., Vernin, J., Azouit, M., Briggs, J. W., Burton, M. G., Ashley, M. C. B., & Manigault, J. F. 1996, A&AS, 118, 385
Marks, R. D., Vernin, J., Azouit, M., Manigault, J. F., & Clevelin, C. 1999, A&AS, 134, 161
Pant, P., & Sagar, R. 1998, Bull. Astron. Soc. India, 26, 397
Pant, P., Stalin, C. S., & Sagar, R. 1999, A&AS, 136, 19
Roddier, F. 1981, Prog. Opt., 19, 281
Short, N., Fitelson, W., & Townes, C. H. 2003, ApJ, 599, 1469
Vernin, J., & Munoz-Tunon, C. 1992, A&A, 257, 811